

Globular Cluster UVIT Legacy Survey (GlobULeS) – II. Evolutionary status of hot stars in M3 and M13

Ranjan Kumar ^{1*}, Ananta C. Pradhan ^{1†}, Snehalata Sahu ²,
Annapurni Subramaniam ³, Sonika Piridi ¹, Santi Cassisi ^{4,5}, Devendra K. Ojha ⁶

¹Department of Physics and Astronomy, National Institute of Technology, Rourkela, Odisha - 769 008, India

²Department of Physics, University of Warwick, Coventry, CV4 7AL, UK

³Indian Institute of Astrophysics, Koramangala II Block, Bangalore-560034, India

⁴INAF - Astronomical Observatory of Abruzzo, Via M. Maggini, sn. 64100 Teramo, Italy.

⁵INFN - Sezione di Pisa, Università di Pisa, Largo Pontecorvo 3, 56127 Pisa, Italy.

⁶Department of Astronomy and Astrophysics, Tata Institute of Fundamental Research (TIFR), Mumbai - 400 005, India

Accepted 2023 March 30. Received 2023 March 16; in original form 2022 September 3

ABSTRACT

We present a far-ultraviolet (FUV) study of hot stellar populations in the second parameter pair globular clusters (GCs) M3 and M13, as a part of the Globular cluster UVIT Legacy Survey program (GlobULeS). We use observations made with F148W and F169M filters of the Ultraviolet Imaging Telescope (UVIT) onboard *AstroSat* along with ground-based data (UBVRI filters), *Hubble Space Telescope* (*HST*) GC catalogue, and *Gaia* EDR3 catalogue. Based on the FUV-optical colour-magnitude diagrams, we classify the sources into the horizontal branch (HB) stars, post-HB stars, and hot white dwarfs (WDs) in both the GCs. The comparison of synthetic and observed colours of the observed HB stars suggests that the mass-loss at the red giant branch (RGB) and He spread in both clusters have a simultaneous effect on the different HB distributions detected in M3 and M13, such that, HB stars of M13 require a larger spread in He (0.247 – 0.310) than those of M3 ($Y = 0.252 - 0.266$). The evolutionary status of HB stars, post-HB stars, and WDs are studied using SED fit parameters and theoretical evolutionary tracks on the H-R diagram. We found that the observed post-HB stars have evolved from zero-age HB (ZAHB) stars of the mass range 0.48 – 0.55 M_{\odot} in M3 and M13. We detect 24 WD candidates in each cluster having $\log(L_{\text{bol}}/L_{\odot})$ in the range –0.8 to +0.6 and $\log(T_{\text{eff}}/K)$ in the range of 4.2 to 5.0. Placing the WDs on the H-R diagram and comparing them with models suggest that M13 has a population of low-mass WDs, probably originating from binary evolution.

Key words: stars: horizontal branch–white dwarf–Hertzsprung–Russell and colour-magnitude diagrams– (Galaxy:) globular clusters: individual: NGC 5272 (M3) and NGC 6205 (M13) – ultraviolet: stars

1 INTRODUCTION

M3 (NGC 5272) and M13 (NGC 6205) are regarded as two twin globular clusters (GCs) in many aspects. They have been studied extensively photometrically, particularly, in optical and ultraviolet (UV) wavebands to explore the peculiar features of their horizontal branch (HB) stars (Newell 1970; Peterson 1983; Laget et al. 1992; Catelan & de Freitas Pacheco 1995; Whitney et al. 1995; Ferraro et al. 1997; Behr 2003; Moehler et al. 2003; Dalessandro et al. 2013; Denis-

senkov et al. 2017; Chen et al. 2021). Despite having similar metallicity ($[Fe/H] \sim -1.5$ dex) and age (~ 12.5 Gyr) (Harris 1996), their HB morphologies are different. In optical colour-magnitude diagrams (CMDs), HB stars of M3 show a horizontal sequence, covering red HB, RR Lyrae (RRL), and blue HB (Ferraro et al. 1997), whereas HB stars of M13 show a vertical sequence, covering extreme HB, blue HB, and a very small number of RRL variables (Paltrinieri et al. 1998). The morphology of HB stars in M3 and M13 has served as the best suitable example of the long-standing “second parameter problem” for decades (Sandage & Wildey 1967; Rood 1973; Catelan & de Freitas Pacheco 1995; Moehler et al. 2003; Dalessandro et al. 2013). Several investigations

* E-mail: ranjankmr488@gmail.com

† E-mail: acp.phy@gmail.com

were carried out to identify the second parameter that governs the HB morphology in Galactic GCs, but not a single parameter is confirmed yet (for a detailed review see [Moehler 2010](#); [Dotter 2013](#); [Milone et al. 2014](#); [Cassisi & Salaris 2020](#); [Milone & Marino 2022](#), and references therein).

Multiple populations (MPs) in GC play a vital role in placing the core He-burning stars of the cluster on the HB. Second-generation (2G) stars are usually He-enhanced ([Milone et al. 2018](#)). They evolve more quickly and lose more mass along the RGB phase than the first-generation (1G) stars which are typically He-normal. As a result, 2G stars on HB have higher effective temperature (T_{eff}) than the 1G stars ([Tailo et al. 2019, 2020](#)). Both the extreme HB stars of M13 and the blue HB stars of M3 are the progeny of 2G RGB stars that are enriched with He and have had considerably greater mass-loss along the RGB phase ([Tailo et al. 2020](#)). With the aid of the multi-band HST globular cluster survey data, there have been numerous advancements made over the past ten years in the study of multiple populations in GCs ([Milone & Marino 2022](#), and references therein). However, their impact on shaping the HB morphology in GCs has been mostly contributed by the variation in He-abundances ([Marino et al. 2014](#); [Brown et al. 2016](#); [Milone et al. 2018](#)) and the mass-loss along the RGB phase of the 1G and 2G populations ([Tailo et al. 2019, 2020](#)).

In the last decade, the observed HB morphology in M3 and M13 was studied by [Dalessandro et al. \(2013\)](#); [Denissenkov et al. \(2017\)](#); [Tailo et al. \(2019\)](#) and [Tailo et al. \(2020\)](#) using He-spread and mass-loss prescriptions. They have all stated that the observed HB sequence in M13 requires a relatively higher He-spread as well as mass-loss than that in M3. In order to produce the observed HB sequence of M3, a similar mass-loss and He-spread is required. In order to produce the observed HB sequence of M13, [Dalessandro et al. \(2013\)](#) reported a He-spread (ΔY) of 0.05 dex with maximum mass-loss along RGB (ΔM) of 0.266 M_{\odot} , [Denissenkov et al. \(2017\)](#) reported ΔY of 0.08 dex with maximum ΔM of 0.2165 M_{\odot} , and [Tailo et al. \(2020\)](#) reported maximum ΔM of $0.273 \pm 0.021 M_{\odot}$ using ΔY of 0.052 ± 0.004 dex derived by [Milone et al. \(2018\)](#). The above-reported values suggest that the estimates of He-spread and mass-loss by [Dalessandro et al. \(2013\)](#) are still valid within the uncertainties of the values derived by [Milone et al. \(2018\)](#) and [Tailo et al. \(2020\)](#) using the latest information on multiple populations in GCs. However, further investigation is certainly required in order to find the best relation between He-spread and mass-loss along RGB in order to produce the HB morphology of Galactic GCs.

Stars in the post-HB phase evolve faster than their previous evolutionary phases, hence, we see a very small number of such stars in GCs. Based on their morphology in the HB phase, the progeny of red HB, blue HB, and extreme HB stars evolve differently. A detailed analysis on the post-HB evolution of stars in GCs can be found in [Moehler et al. \(2019\)](#), [Bond \(2021\)](#), and [Davis et al. \(2022\)](#). The number and nature of post-HB stars in M3 and M13 are different due to their dissimilar morphology in the HB phase. In the case of M3, HB stars are mostly dominated by red HB to cooler blue HB stars whereas post-HB stars are mostly dominated by AGB stars ([Chen et al. 2021](#)). Seven AGB-manqué stars were detected in M13 by [Chen et al. \(2021\)](#) and also they found a relatively smaller fraction of AGB/HB ratio in M13

(0.08 ± 0.01) than in M3 (0.13 ± 0.02). However, there is no proper statistics on the AGB-manqué or hotter post-HB stars yet in these two clusters. This issue might be resolved with UV photometry as in UV they are relatively brighter and easily identifiable than in optical photometry.

The different stellar evolutionary scenarios of the progenitors are likely to affect their white dwarf (WD) population as well. By analysing the high-resolution photometric data of *HST*, [Chen et al. \(2021\)](#) found an overabundance (1.5 times) of bright WDs in M13 in comparison to M3. From their theoretical models, they argued that the observed overabundance of WDs in M13 might be due to an excess of extreme HB stars in M13 and subsequently a larger fraction of post-HB stars which do not reach the AGB phase (i.e., PEAGB/AGB-manqué stars which do not experience the third dredge-up). Such stars might retain an excess amount of hydrogen on their surface which is burned through a stable nuclear reaction during their WD cooling phase ([Miller Bertolami et al. 2013](#); [Althaus et al. 2015](#)). This excess hydrogen burning slows down the WD cooling process which delays the cooling time of such stars and hence we observe a larger fraction of WDs at their hotter/brighter end of the cooling sequence. An UV analysis of WDs in M3 and M13 will certainly benefit to test this theory.

The Ultraviolet Imaging Telescope (UVIT) onboard *AstroSat* has been playing an important role in exploring the hot HB stars in UV in several GCs. Using UVIT filters, [Kumar et al. \(2022\)](#) detected two new hot sources in M68; one extreme HB star and a post-blue hook star. [Kumar et al. \(2021a,b\)](#) studied the hot blue HB populations in two, GCs NGC 4147 and NGC 7492, and detected one new extreme HB star in NGC 7492. [Prabhu et al. \(2021\)](#) studied the physical properties of post-HB stars in NGC 2808 and segregated them into different evolutionary phases such as AGB-manqué, PEAGB, post-AGB, etc. Hot stellar populations such as extreme HB stars, hot WD binaries, blue stragglers, etc., have been studied in two GCs, NGC 288 and NGC 1851 by [Sahu et al. \(2019\)](#) and [Singh et al. \(2020\)](#), respectively using UVIT photometry. Recently, [Sahu et al. \(2022\)](#) have made a comprehensive study of UV bright sources in 11 GCs and prepared a photometric catalogue of the sources up to 23.5 mag in F148W filter of UVIT. They were able to detect Grundahl jump (G-jump; [Grundahl et al. 1998](#)) and Momany jump (M-jump; [Momany et al. 2004](#)) corresponding to T_{eff} 11,500 K and 21,000 K in HB stars of M13 using pseudo colour ($F148W_{\text{UVIT}} - 2 \times F336W_{\text{HST}} + F606W_{\text{HST}}$) versus colour ($F148W_{\text{UVIT}} - F606W_{\text{HST}}$) plot. In this paper, we aim to perform a comprehensive study of the HB morphology of M3 and M13 GCs and explore their further evolutionary status, such as AGB-manqué, PEAGB, post-AGB and hence, the final product, WDs, in both the clusters.

We present the data reduction and photometry procedures of the UVIT observation of M3 and M13 in §2. In §3, we discuss the UV-optical CMDs and the classification of sources. In §4, a validation of He-spread on the HB of M3 and M13 is performed by comparing the observed HB stars with synthetic HB stars. In §5, we have explored the evolutionary status of the post-HB stars. In §6, we have studied the spectral energy distribution (SED) of WD candidates and discussed their evolutionary scenario. Finally, we have concluded our results in §7.

2 OBSERVATION AND DATA REDUCTION

We observed M3 and M13 in two FUV filters, F148W and F169M of UVIT. The exposure times of M3 (M13) are 3,000 (6,654) and 2,883 (6,657) seconds in F148W and F169M filters, respectively. The observation, photometry, and cluster membership details of the observed sources are provided in Sahu et al. (2022). The total number of sources detected in M3 and M13 are 878 and 1090, respectively. The completeness of the observed sources in M3 and M13 is above 90% each outside the half-light radius (r_h) of the clusters, and it is 80 - 90% and 60 - 70%, respectively, for sources in between core-radius (r_c) and r_h of the clusters, and $\sim 50\%$ each for sources within r_c , respectively. The sources present in the inner region i.e., within $3.5' \times 3.5'$ of the cluster core were cross-matched with *HST* GC catalogue (Nardiello et al. 2018) and the rest of the sources beyond this core region were cross-matched with *Gaia* EDR3 catalogue (Vasiliev & Baumgardt 2021). We retain only those sources which have a cluster membership probability of more than 90% in the catalogue. Finally, we were left with 274 (399) stars in the inner region (*HST* counterparts) and 160 (390) stars in the outer region (*Gaia* counterparts) of the cluster M3 (M13). The *Gaia* counterparts were then cross-matched with the ground-based photometric catalogue to obtain the magnitudes in U, B, V, R, and I filters (Stetson et al. 2019). All the observed sources were extinction corrected using the extinction values ($E(B - V) = 0.011$ mag for M3 and 0.014 mag for M13) obtained from dust extinction map of Schlafly & Finkbeiner (2011) and extinction law of Cardelli et al. (1989).

3 COLOUR-MAGNITUDE DIAGRAMS

The optical CMDs for all the cluster members in the inner (within $3.5' \times 3.5'$ of the core and detected by *HST*) and outer (beyond $3.5' \times 3.5'$ of the core and observed by ground-based telescopes in UBVRI filters) regions of both the clusters are shown in Figure 1 (M3: top panels and M13: bottom panels). The cluster members with membership probability $> 90\%$ and observed with both *HST* (left panels) and UBVRI filters (right panels) are marked with gray solids. UVIT observed cross-matched sources are over-plotted in black solids. Sources shown in blue solids are FUV-detected sources for which the membership probability is not available (except a few, observed with *HST* in the inner region of the cluster), however, their positions in optical CMDs lie in the WD region, i.e., 3 - 4 magnitudes fainter than main-sequence turn-off. Considering these sources as probable WD candidates, we discuss them later in this paper. The BaSTI-IAC isochrones and zero age HB (ZAHB) locus (Pietrinferni et al. 2021) are over-plotted in the CMDs which are scaled to the observed plane using distance moduli of 15.02 mag and 14.42 mag for M3 and M13, respectively (Denissenkov et al. 2017).

We generated the isochrones and ZAHB locus for M3 using $[\text{Fe}/\text{H}] = -1.55$ dex, $[\alpha/\text{Fe}] = 0.4$ dex, age = 12.6 Gyr and two different values of Y (0.248 and 0.275). As seen in Figure 1, the isochrone with $Y = 0.248$ (red solid line) is fitting well with the red HB region and the isochrone with $Y = 0.275$ (blue solid line) is lying in the blue HB region in CMDs of M3. But the isochrone with $Y = 0.275$ is not

able to cover the magnitude spread of blue HB stars (i.e., the observed HB magnitude spread, 15.2 - 19.8 (14.8 - 19.2) mag in the F606W filter for the inner region and 15.2 - 20.0 (14.8 - 19.2) mag in the V filter for the outer region of the cluster M3 (M13)). However, the ZAHB locus with $Y = 0.300$ (green solid lines in the upper panels of Figure 1) is fitting well with the observed HB sequences in the inner as well as outer regions of M3. The bottom panels of Figure 1 show the optical CMDs for M13. The over-plotted isochrones and ZAHB locus in the figure are generated for $[\text{Fe}/\text{H}] = -1.55$, $[\alpha/\text{Fe}] = 0.4$, age = 12.9 Gyr, and $Y = 0.300$ which fit well with the observed optical CMDs.

Figure 2 shows the UV-optical CMDs of GCs M13 and M3. We use UVIT F148W and *HST* F606W filters for the CMDs of inner regions whereas UVIT F148W and ground-based V filters for the CMDs of outer regions of the clusters. We superpose the BaSTI-IAC ZAHB loci for $Y = 0.248$ (black solid line), $Y = 0.300$ (green solid line) and terminal age HB (TAHB) locus for $Y = 0.300$ (green dashed line) on the CMDs. The ZAHB and TAHB loci are scaled to the observed plane as mentioned earlier. Labels in the figure represent the position of stars of different evolutionary phases. We notice a tight HB sequence along the ZAHB locus in both clusters. We assign stars above the TAHB locus (above the green dashed line) as post-HB stars (brown diamonds). The group of stars (black diamonds) located below the HB sequence are probable WDs. The stars below the HB sequence marked with violet diamonds are blue-straggler (BS) stars, as suggested in Schiavon et al. (2012) and Sahu et al. (2022).

The observed HB sequence in Figure 2 ranges from blue HB to extreme HB phase ($7,500 \text{ K} \leq T_{\text{eff}} \leq 30,000 \text{ K}$) which has two prominent discontinuities (also known as gaps, jumps, over-luminous stars, or sub-luminous stars in different colours), the ‘‘Grundahl jump’’ (G-jump) within the blue HB at $\sim 11,500 \text{ K}$ (Grundahl et al. 1998, 1999) and the ‘‘Momany jump’’ (M-jump) within the extreme HB at $\sim 20,000 \text{ K}$ (Momany et al. 2002, 2004). HB stars in between G-jump and M-jump (i.e., within T_{eff} range 11,500 K to 20,000 K) suffer from radiative levitation in the stellar atmosphere (increase in abundances of metal species like Fe, Cr, and Ti around solar or higher) and gravitational settling (depletion of He abundance by a factor of 10 or more) (Behr 2003; Moehler et al. 2003; Brown et al. 2016). Hence, we divide the observed HB stars on the basis of temperature into three sub-populations -

blue-HB (bHB): $7,750 \text{ K} \leq T_{\text{eff}} \leq 11,500 \text{ K}$

intermediate-HB (iHB): $11,500 \text{ K} \leq T_{\text{eff}} \leq 20,000 \text{ K}$

extreme-HB (eHB): $20,000 \text{ K} \leq T_{\text{eff}} \leq 30,000 \text{ K}$

We have used BaSTI-IAC ZAHB locus to co-relate the T_{eff} of HB stars with different UV-optical colours as shown in Figure 2. The F148W-F606W (F148W-V) colours at T_{eff} 7,750 K, 11,500 K, 20,000 K, and 30,000 K are 5.22 (5.23), 1.12 (1.17), -0.86 (-0.79), and -1.89 (-1.81), respectively and these colours or temperatures are marked in gray vertical lines on the HB sequence. We have also marked the corresponding HB masses (M_{HB}) at these T_{eff} values in the CMDs. The M_{HB} values corresponding to T_{eff} of 7,500 K, 11,500 K, 20,000 K, and 30,000 K are $0.65 M_{\odot}$, $0.60 M_{\odot}$,

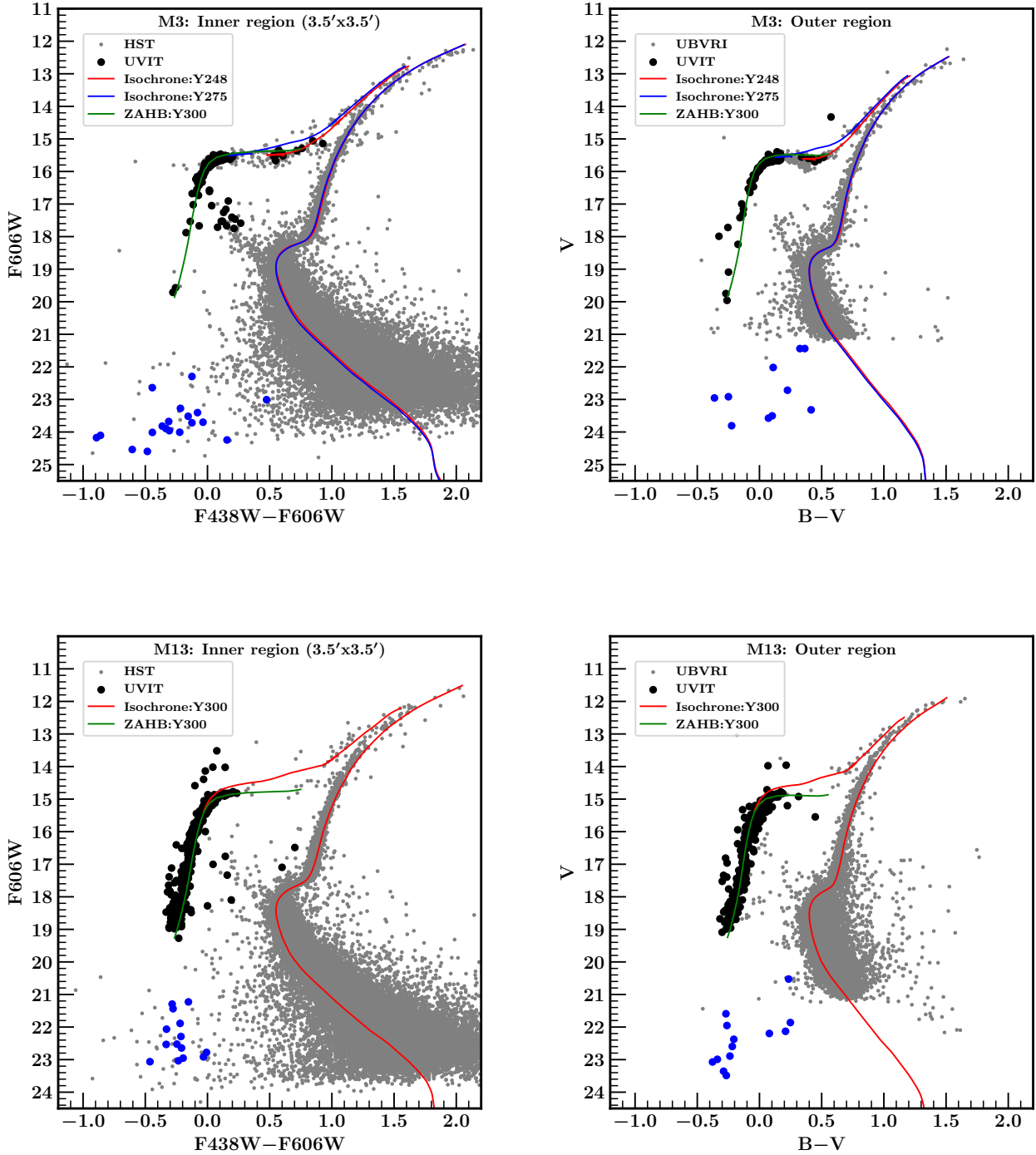


Figure 1. Optical CMDs of M3 (upper panels) and M13 (lower panels) for *HST* GCs catalogue (left panels) and UVBRI photometry data (right panels). The overall cluster members with membership probability $> 90\%$ are shown in gray solids and the cross-matched UVIT counterparts are shown in black solids. UVIT observed WDs are denoted by blue solids. The red and blue coloured isochrones in the top panels are obtained for $Y = 0.248$ and 0.275 , respectively, for GC M3 and the red coloured isochrones in the bottom panels are for $Y = 0.300$ of M13. The ZAHB locus of $[\text{Fe}/\text{H}] = -1.55$, $[\alpha/\text{Fe}] = +0.4$, and $Y = 0.300$ (green line) is shown in both the clusters. The physical parameters are taken from [Denissenkov et al. \(2017\)](#).

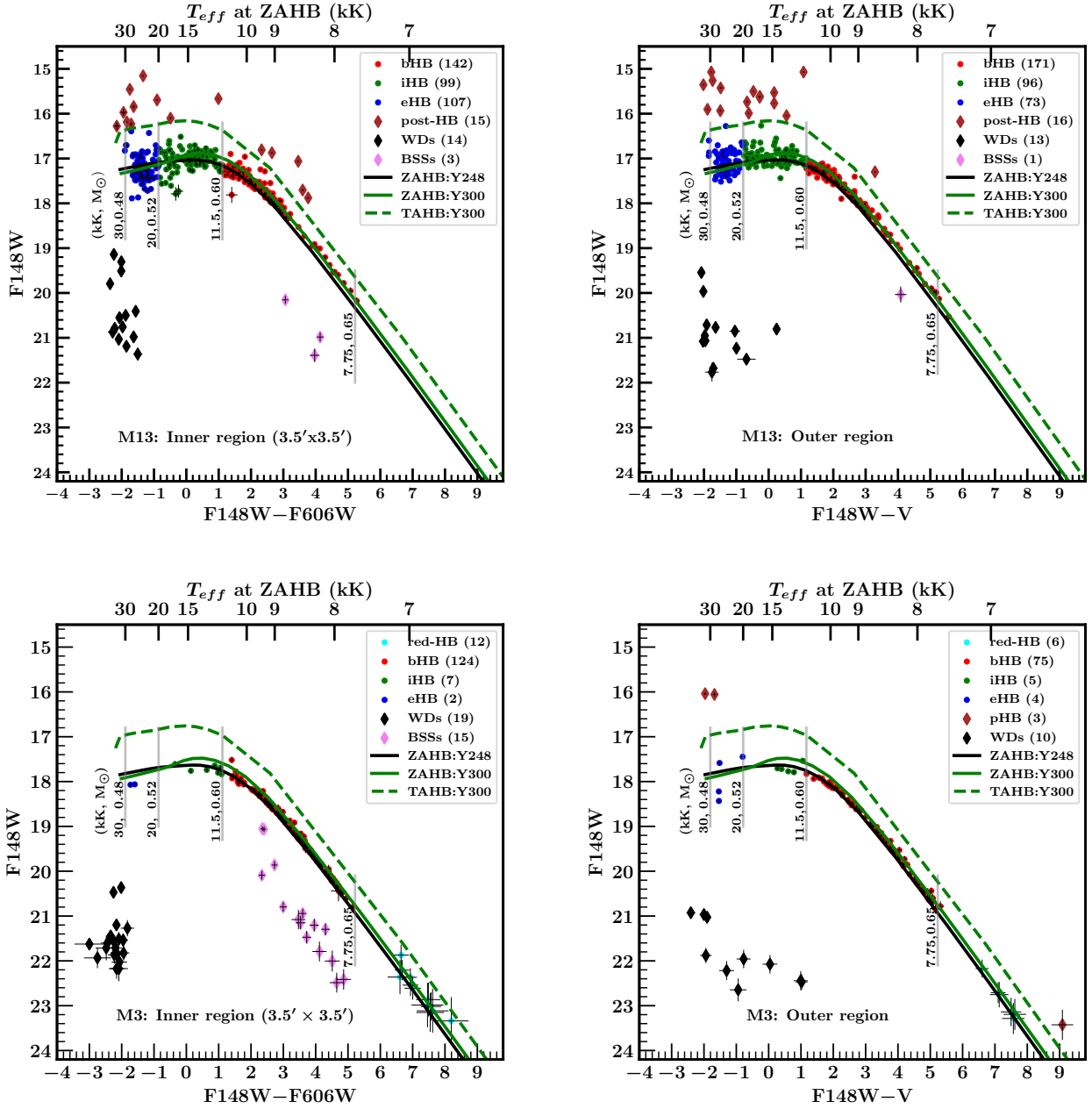


Figure 2. UV-optical CMDs of M13 (upper panels) and M3 (lower panels). The left panels show the CMDs of observed stars at the core (in the $3.5' \times 3.5'$ central region), and the right panels show the CMDs of the observed stars in the outer region of the clusters. Stars of different evolutionary phases (along with their respective counts) are shown by different symbols as mentioned in the legend. The ZAHB loci of $Y = 0.248$ and $Y = 0.300$ are represented by black and green solid lines. The TAHB locus of the $Y = 0.300$ model is shown in the dashed green line. Different colour regions along the observed HB sequence are marked with vertical gray lines (see text for details). The T_{eff} (in kK) and M_{HB} (in M_{\odot}) of HB stars at the boundary of HB sub-populations are also indicated on the left of the vertical gray lines. The error bars in colour and magnitude of the observed stars are overlaid as black cross lines.

0.52 M_{\odot} , and 0.48 M_{\odot} , respectively. The UVIT observed stars in bHB, iHB, and eHB regions are shown in red, green and blue solids, respectively.

As observed in Figure 2, HB stars in M3 are mostly populated in the bHB region (with very few stars in iHB and eHB regions) whereas HB stars in M13 significantly populate the iHB and eHB regions (counts of HB stars in different sub-populations can be found in the legends of Figure 2). We also

found a significant fraction of stars below the ZAHB locus in the eHB and iHB regions in M13. The observed fraction of stars below the ZAHB locus in the iHB region might be due to a higher Fe abundance than the cluster metallicity (Moehler et al. 2003) whereas the fractional increase of eHB stars below ZAHB may be due to the fact that either they would be blue-hook (BHk) stars or eHB stars with higher Y

than the considered Y for the plotted ZAHB in the figure (Prabhu et al. 2021; Sahu et al. 2022).

4 HELIUM SPREAD ON HB STARS OF M3 AND M13

We have investigated the He-spread on the HB stars bluer than the RRL gap by comparing their synthetic CMDs with the observation as shown in Figure 3. We have adopted the methods provided by Dalessandro et al. (2013) to generate the synthetic magnitudes of HB stars in UVIT, *HST* and UBVR filters. Calculation of synthetic magnitudes of HB stars requires specification of their chemical composition, He-spread, and mass-loss in the RGB phase.

The synthetic colours and magnitudes for HB stars in the M3 cluster are generated using $Y = 0.246$, $\Delta Y = 0.02$ (uniform distribution), RGB total mass-loss $\Delta M = 0.122 M_{\odot}$ with a spread in mass-loss governed by $\sigma(\Delta M) = 9.0 \times (Y - 0.246) M_{\odot}$, where Y is the actual initial He mass fraction of the synthetic star. The dependence of $\sigma(\Delta M)$ on Y implies an increase of the mass-loss spread with increasing Y . In the upper panels of Figure 3, we have shown the synthetic and observed HB stars of M3 in red and gray solids, respectively. The observed colours of HB stars are matching well with the synthetic colours (F148W – F606W for the inner and F148W – V for the outer regions of the cluster) in the bHB region, whereas there is a deviation between them in eHB and iHB regions.

Similarly, the synthetic colours and magnitudes for HB stars in M13 are generated using the best-fitted Y and ΔM parameters derived by Dalessandro et al. (2013) which covers the following ranges of Y and ΔM :

- (i) $Y = 0.246$ to 0.256 (uniform distribution), and $\Delta M = 0.21 M_{\odot}$ with $\sigma(\Delta M) = 0.01 M_{\odot}$ (Gaussian distribution): denoted by red solids in the lower panels of Figure 3.
 - (ii) $Y = 0.285 \pm 0.012$ (Gaussian distribution), and $\Delta M = 0.235 M_{\odot}$ with $\sigma(\Delta M) = 0.01 M_{\odot}$ (Gaussian distribution): denoted by green solids in the lower panels of Figure 3.
 - (iii) $Y = 0.300 \pm 0.003$ (Gaussian distribution), and $\Delta M = 0.266 M_{\odot}$ with $\sigma(\Delta M) = 0.002 M_{\odot}$ (Gaussian distribution): denoted by blue solids in the lower panels of Figure 3.
- We noticed that the observed colours (gray solids) match well with the synthetic colours in the bHB region whereas there is a deviation between the colours in both iHB and eHB regions. Almost 40% of the observed eHB and iHB stars are slightly fainter in F148W magnitudes than the corresponding synthetic values.

The observed and synthetic F148W – F606W colours in the lower panels of Figure 3 suggest that bHB stars in M13 are distributed with Y in the range 0.246 to 0.256. The iHB stars are distributed with Y in the range 0.270 to 0.300 (green solids). The eHB stars have He-distribution in the range of 0.290 to 0.310 (blue solids). Denissenkov et al. (2017) have also studied the HB stars of M3 and M13 GCs using synthetic colours of optical filters. However, they used synthetic HB stars with a relatively larger spread in Y than in ΔM . Their best fit models for M3 suggest $Y = 0.250$, $\Delta Y \sim 0.01$, and $\Delta M = 0.13 M_{\odot}$. Whereas synthetic HB models used in this paper for M3 are $Y = 0.246$, $\Delta Y \sim 0.02$, and $\Delta M = 0.122 M_{\odot}$. These simulations are able to produce similar colours and magni-

tudes in FUV-optical CMDs as observed in bHB stars of M3. The best-fit models in Denissenkov et al. (2017) for M13 suggest $Y = 0.250$, $\Delta Y \sim 0.08$, and $\Delta M = 0.2 M_{\odot}$. Whereas synthetic HB models used in this paper for M13 are $Y = 0.246$, $\Delta Y \sim 0.06$, and $\Delta M = 0.266 M_{\odot}$. The observed HB stars in M13 in UV-optical CMDs cover the colour range, however, the UV magnitudes of simulated HB stars are brighter than the observed HB stars in eHB and iHB regions. The comparison of synthetic and observed colours of HB stars suggests that the mass-loss at RGB and initial He-spread in both clusters have a simultaneous effect on the different HB distributions observed in M3 and M13. e.g., HB stars of M13 require a larger spread in Y as well as ΔM . M13 with a larger fraction of eHB and iHB stars than M3 can only be simulated if HB distribution has higher values of Y and ΔM .

4.1 Multiple populations along RGB and their impact on HB morphology of M13 and M3

The chromosome maps of M13 have revealed that it consists of a long sequence of 2G stars and a small number of 1G stars along the RGB (Figure 5 of Milone et al. 2017) with a fraction of 0.184 ± 0.013 1G RGB stars. The UVIT observed HB sequence of M13 starts from the bluer side of the RRL stars (with a small number of RRL stars residing towards the bluer end of the instability strip; see Figure 1). This suggests that $\sim 18\%$ of the observed blue HB stars (including RRL stars) would be the progeny of the 1G RGB stars. Hence, to reproduce them, initial He-abundance $Y \sim 0.25$ dex and respective RGB mass-loss $\Delta M = 0.210 M_{\odot}$ of 1G stars would be required (Milone et al. 2018; Tailo et al. 2020). A similar initial He abundance and mass-loss values have been used in Dalessandro et al. (2013) and also in our present work, i.e, $Y \sim 0.246$ to 0.256 dex and $\Delta M = 0.210 M_{\odot}$ to reproduce the blue HB stars near the RRL strip.

The eHB stars (the bluest and the hottest HB stars) were reproduced by Tailo et al. (2020) using an enhanced He-abundance ($\delta Y_{\max} = 0.052 \pm 0.004$) and a higher mass-loss at RGB ($\Delta M = 0.273 \pm 0.021 M_{\odot}$). Milone et al. (2018) suggested that such an extreme He enrichment represents the extreme 2G (2Ge, bluest 2G RGB) stars in the chromosome map (Figure 2 of Milone et al. 2018). Hence, the extreme HB stars would be the progeny of 2Ge RGB stars. Dalessandro et al. (2013) have used a similar prescription of He enhancement ($\Delta Y = 0.05$) and mass-loss along RGB stars ($\Delta M = 0.266 M_{\odot}$) to reproduce the extreme HB stars of M13 and we have used their values in our work.

A comparison between the observed and simulated HB sequences (lower panels of Figure 3) suggests that the overall observed UV-optical colours are covered by the simulated stars with three different He and RGB mass-loss prescriptions. However, the observed and simulated HB number counts are not matching well when using the Gaussian distribution of He-abundance (with $Y_{\text{mean}} = 0.285$ and 0.300) and RGB mass-loss ($\Delta M_{\text{mean}} = 0.235 M_{\odot}$ and $0.266 M_{\odot}$). Hence, we suggest a uniform distribution of He and mass-loss along RGB would be more efficient in producing the observed star counts along the HB sequence.

The average and maximum value of He enhancement between 1G and 2G RGB stars of M3 as estimated by Milone et al. (2018) are $\Delta Y_{1G,2G} = 0.016 \pm 0.005$ and $\delta Y_{\max} =$

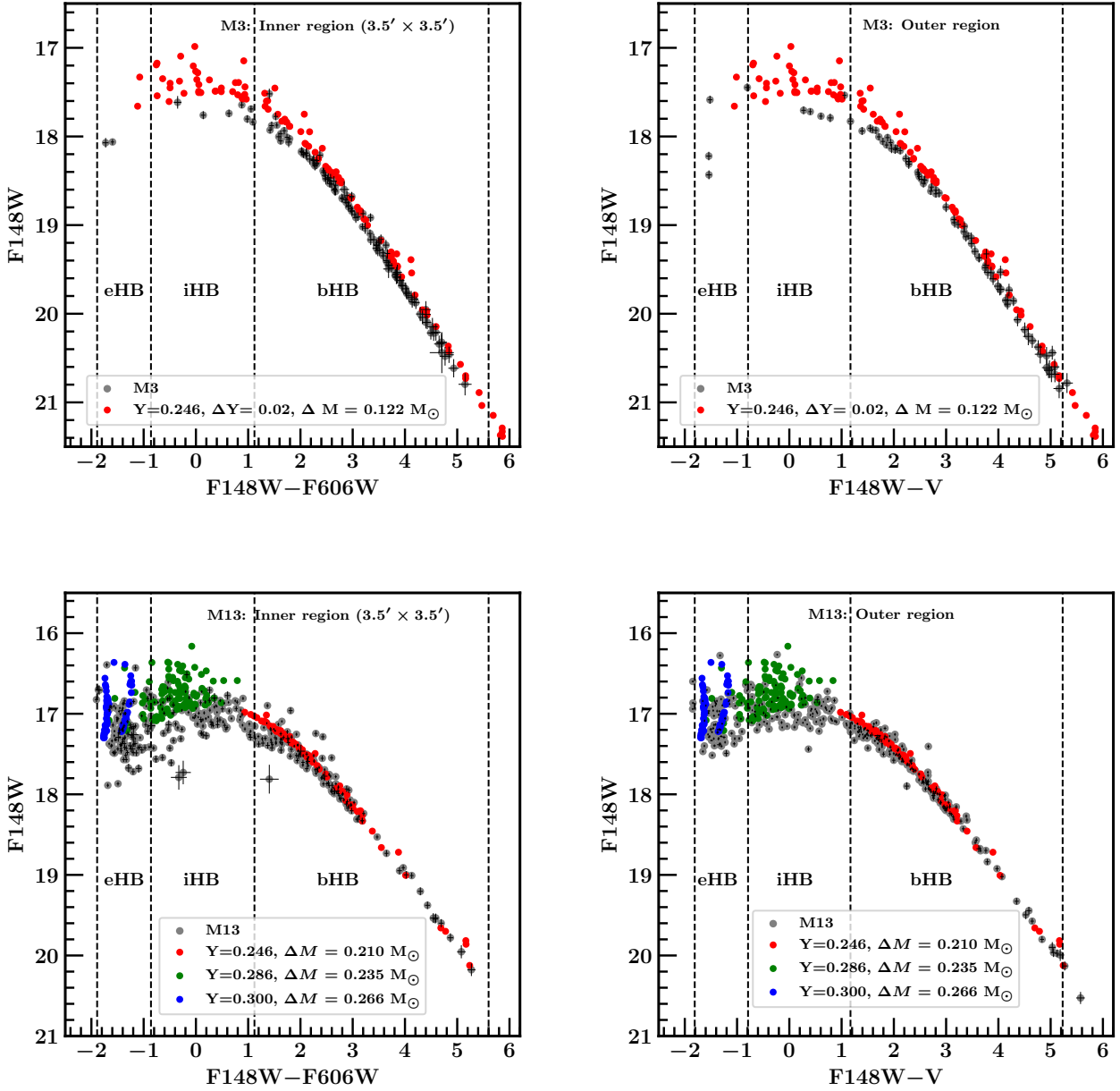


Figure 3. UV-optical CMDs of inner and outer regions of M3 and M13 as mentioned on the top of the respective panels. Gray solids represent the observed sources. Red solids in top panels are synthetic HB stars for $Y = 0.246 - 0.265$ and mass-loss at RGB-tip $\Delta M = 0.122 M_{\odot}$. Red, green, and blue solids in bottom panels are synthetic HB stars for Y and $\Delta M = (0.246, 0.210 M_{\odot})$, $(0.286, 0.235 M_{\odot})$, and $(0.300, 0.266 M_{\odot})$, respectively. The sub-populations of bHB, iHB, and eHB are indicated by vertical dashed lines.

0.041 ± 0.009 , respectively. These values are used by [Tailo et al. \(2019\)](#) to estimate the mass-loss of RGB stars to reproduce the HB stars of M3. They divided the observed blue HB stars of M3 into three groups: $2G_A$, $2G_B$, and $2G_C$ with the $2G_A$ group having the greatest amount of blue HB stars. The assigned He enhancement for $2G_A$ stars are $\Delta Y_{1G,2G}$ ($Y_{1G} = 0.25$), $2G_C$ stars are δY_{\max} , and $2G_B$ stars are in the range between $\Delta Y_{1G,2G}$ and δY_{\max} . Their best fitted results indicate RGB mass-loss of $0.204 M_{\odot}$, $0.220 M_{\odot}$, $0.240 M_{\odot}$ in $2G_A$, $2G_B$, and $2G_C$ HB stars, respectively. The blue HB

stars of M3 that we study here are split into three categories (bHB, iHB, and eHB stars). [Figure 3](#) and [4](#) show that the He-spread of 0.252 to 0.266 ($\Delta Y = 0.16$ taking $Y_{1G} = 0.25$) is a good fit for the bHB stars and is similar to the $2G_A$ population fitted by [Tailo et al. \(2019\)](#). The iHB stars of M3 match well with a He-abundance of 0.258 to 0.266, which is comparable to the $2G_B$ HB population identified by [Tailo et al. \(2019\)](#), and can be used to fit the iHB stars of M3. To replicate the eHB stars of M3 that mirror the $2G_C$ population in [Tailo et al. \(2019\)](#), it is unquestionably

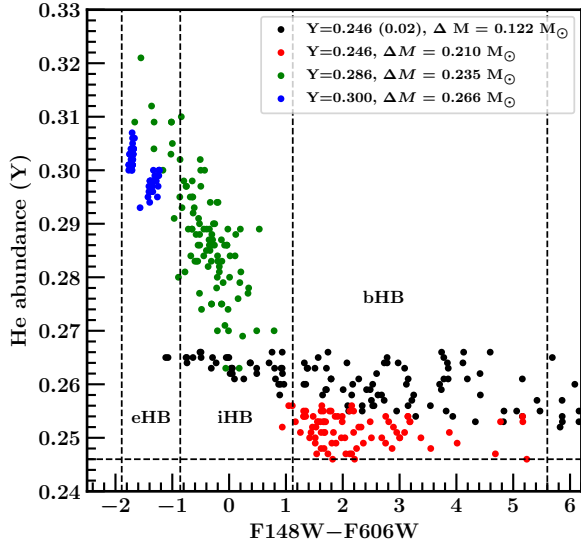


Figure 4. F148W – F606W vs. He-spread plot for synthetic HB stars. Synthetic HB stars used to compare the observed HB stars in M13 are shown in red, green, and blue solids as described in the legends for different combinations of He-spread and mass-loss on RGB. The black solids are synthetic HB stars used to compare the observed HB stars of M3. bHB, iHB, and eHB sub-populations are indicated by vertical dashed lines. The horizontal dashed line shows the canonical He-abundance ($Y_{init} = 0.247$).

necessary to increase He-abundance and mass-loss values. Here, we note that we have used relatively lower values of mass-loss ($\Delta M = 0.122 M_{\odot}$) and a spread in mass-loss using equation $\sigma(\Delta M) = 9.0 \times (Y - 0.246)$ in the blue HB stars as compared to [Tailo et al. \(2019\)](#). The simulated HB stars match well with the observed colour spread in the bHB stars of M3 ([Figure 3](#)).

Recently, it has been shown that in many GCs there is a spread in the $[\text{Fe}/\text{H}]$ abundances in the 1G RGB stars ([Marino et al. 2019](#); [Lardo et al. 2022](#); [Legnardi et al. 2022](#); [Lardo et al. 2023](#)) as obtained on the basis of the colour distribution of stars in the chromosome map. However, the UVIT observed HB stars of M3 and M13 are blue HB stars which are the progeny of the 2G RGB population, hence the variation in their metallicity should be small as stated by [Legnardi et al. \(2022\)](#). Hence, the iron spread in the 1G RGB population of the clusters will not affect the present analysis of blue HB stars of M3 and M13.

5 HOT POST-HB STARS IN M3 AND M13

The post-HB stars when evolving from eHB and iHB regions become brighter in UV filters and appear as a vertical sequence above eHB and iHB stars in the UV-optical CMDs ([Schiavon et al. 2012](#); [Dalessandro et al. 2013](#); [Moehler et al. 2019](#); [Prabhu et al. 2021](#)). Although [Dalessandro et al. \(2013\)](#) indicated the presence of post-HB stars in M13 using *HST* data, they did not provide any detailed statistics about them. We have used F148W–F606W vs F148W CMD for the inner region (left panels of [Figure 2](#)) and F148W–V vs

F148W CMD for the outer region (right panels of [Figure 2](#)) of the clusters to identify post-HB stars. We identified a total of 31 post-HB stars in M13 and 3 post-HB stars in M3 which are brighter than the observed HB stars in F148W filters at the similar $(\text{F148W} - \text{F606W}) / (\text{F148W} - \text{V})$ colours. There are 15 (16) post-HB stars in the inner (outer) region of M13. They all appear to be distributed above the eHB, iHB, and bHB stars. Recently, [Davis et al. \(2022\)](#) have reported 13 post-HB stars in M13 considering stars above HB region, spanning from red HB to bHB, in optical (V–I vs. V) CMDs. Such stars have originated from bHB or red HB stars of the cluster ([Moehler et al. 2019](#)). However, we see a possibility of a large number of post-HB stars evolving from the populated eHB and iHB in M13. [Chen et al. \(2021\)](#) have mentioned only about 7 post-HB stars evolving from the eHB region while studying the inner region of the cluster with the *HST* F275W filter (which is a near-UV filter). We have detected all the 7 reported post-HB stars in [Chen et al. \(2021\)](#) along with additional 24 post-HB stars in the inner as well as outer regions of M13.

In M3, we could observe post-HB stars only in the outer region of the cluster. Out of the 3 post-HB stars in M3, 2 are above the eHB, and 1 above the red HB. This suggests that only 2 post-HB stars are evolving from the eHB in M3. [Schiavon et al. \(2012\)](#) have found 2 AGB-manqué and 1 PEAGB stars in M3. The 2 post-HB stars identified above eHB are the 2 AGB-manqué stars detected by [Schiavon et al. \(2012\)](#). The PEAGB star of [Schiavon et al. \(2012\)](#) is saturated in UVIT images hence we had to exclude it from our analysis.

5.1 Evolutionary status of post-HB stars in M3 and M13

By adopting the BaSTI-IAC stellar model library, we retrieved the post-ZAHB evolutionary tracks for various M_{HB} , $[\text{Fe}/\text{H}] = -1.55$ dex, $[\alpha/\text{Fe}] = 0.4$ dex, and $Y = 0.300$. The evolutionary tracks for $M_{\text{HB}} = 0.485 M_{\odot}$, $0.49 M_{\odot}$, $0.50 M_{\odot}$, $0.52 M_{\odot}$, $0.55 M_{\odot}$, and $0.60 M_{\odot}$ along with TAHB and ZAHB loci are plotted in [Figure 5](#). It is clear from the figure that the evolutionary track of $M_{\text{HB}} = 0.55 M_{\odot}$ (violet solid line) is lying just above the TAHB locus (green dashed line) and the evolutionary track of $M_{\text{HB}} = 0.60 M_{\odot}$ (violet dashed line) lying below the TAHB locus. This suggests that we can identify only those post-HB stars which have evolved from $M_{\text{HB}} \leq 0.55 M_{\odot}$ and post-HB stars evolved from higher M_{HB} would be indistinguishable from HB stars in the UV-optical CMDs. As proposed by [Pietrinferni et al. \(2006\)](#) and [Chen et al. \(2021\)](#), stars with $M_{\text{HB}} \leq 0.55 M_{\odot}$ will never reach the tip of AGB (and hence do not experience any thermal pulse or the third dredge up) and will further evolve through the PEAGB phase. Hence, the observed post-HB stars in [Figure 5](#) will evolve through either PEAGB or AGB-manqué phase. We confirm that there are 31 post-HB stars in M13 and 3 post-HB stars in M3 which have evolved from the low mass HB stars (i.e., eHB and iHB stars, $M_{\text{HB}} \leq 0.55 M_{\odot}$). In [Table 1](#), we list the number of post-HB stars that evolved from the ZAHB locus having different HB mass ranges.

5.2 SED of HB and post-HB stars

We performed spectral energy distribution (SED) fitting on HB and post-HB stars of M3 and M13 using observed

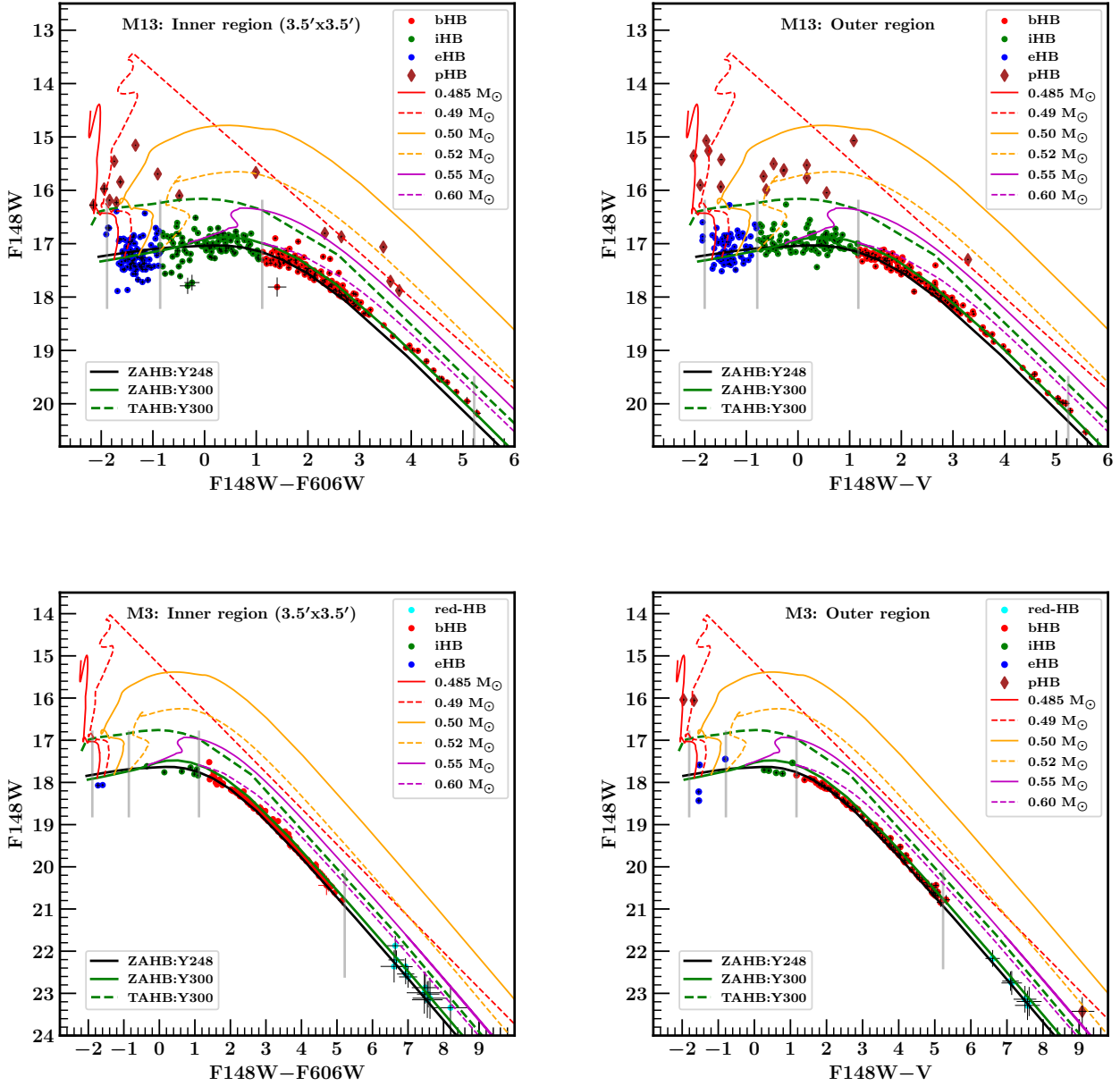


Figure 5. UV-optical CMDs of the UVIT observed sources of inner and outer regions of M13 and M3 as mentioned on the top of the respective panels. Post-ZAHB evolutionary tracks from the BaSTI-IAC model are for ZAHB mass of $0.485 M_{\odot}$ (red solid line), $0.49 M_{\odot}$ (red dashed line), $0.50 M_{\odot}$ (yellow solid line), $0.52 M_{\odot}$ (yellow dashed line), $0.55 M_{\odot}$ (violet solid line), and $0.60 M_{\odot}$ (violet dashed line). The green and black solid lines are ZAHB locus of initial He-abundance $Y = 0.248$ and $Y = 0.300$ respectively. The green dashed line represents the locus of TAHB.

Table 1. Number of post-HB stars in M3 and M13 evolved from ZAHB locus with $M_{\text{HB}} \leq 0.55 M_{\odot}$.

Cluster name	region	Number of post-HB stars evolved from different HB mass range			
		$M_{\text{HB}} \leq 0.49 M_{\odot}$	$0.49 M_{\odot} \leq M_{\text{HB}} \leq 0.50 M_{\odot}$	$0.50 M_{\odot} \leq M_{\text{HB}} \leq 0.52 M_{\odot}$	$0.52 M_{\odot} \leq M_{\text{HB}} \leq 0.55 M_{\odot}$
M13	inner	2	5	3	5
	outer	4	2	7	3
M3	inner	-	-	-	-
	outer	1	1	-	1

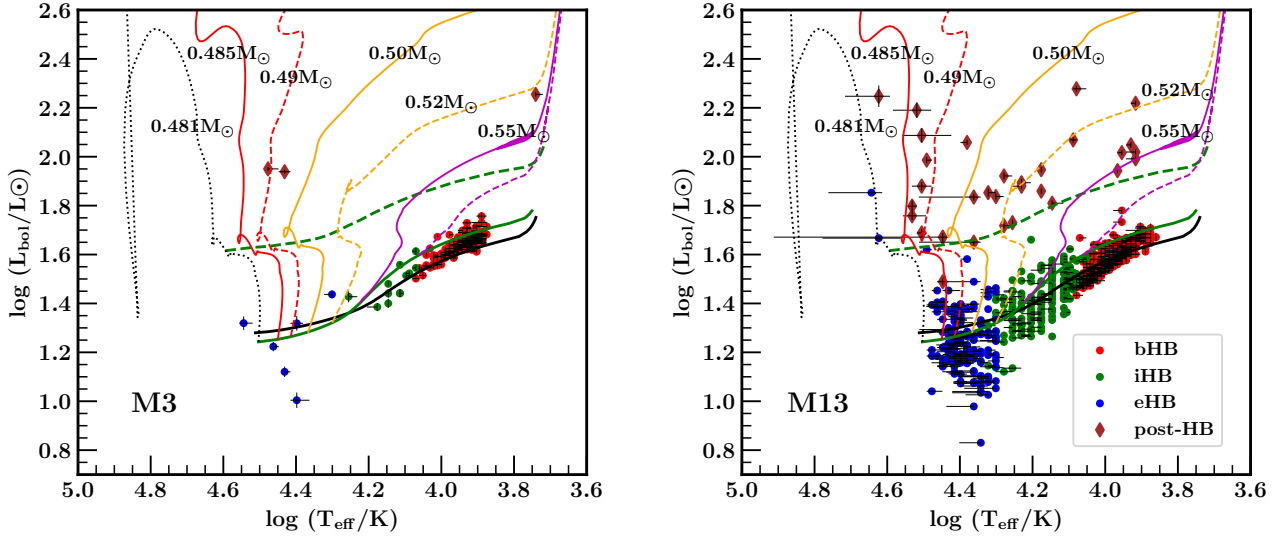


Figure 6. T_{eff} vs luminosity of HBs and post-HBs of M3 (left panel) and M13 (right panel). Various post-ZAHB evolutionary tracks of HB stars in the mass range $0.48 - 0.55 M_{\odot}$, ZAHB and TAHB of $Y = 0.300$, and ZAHB of $Y = 0.248$ are shown in similar colours and styles as that of Figure 5. The post-ZAHB evolutionary track for $M_{\text{HB}} = 0.481 M_{\odot}$ is shown in a black dotted line.

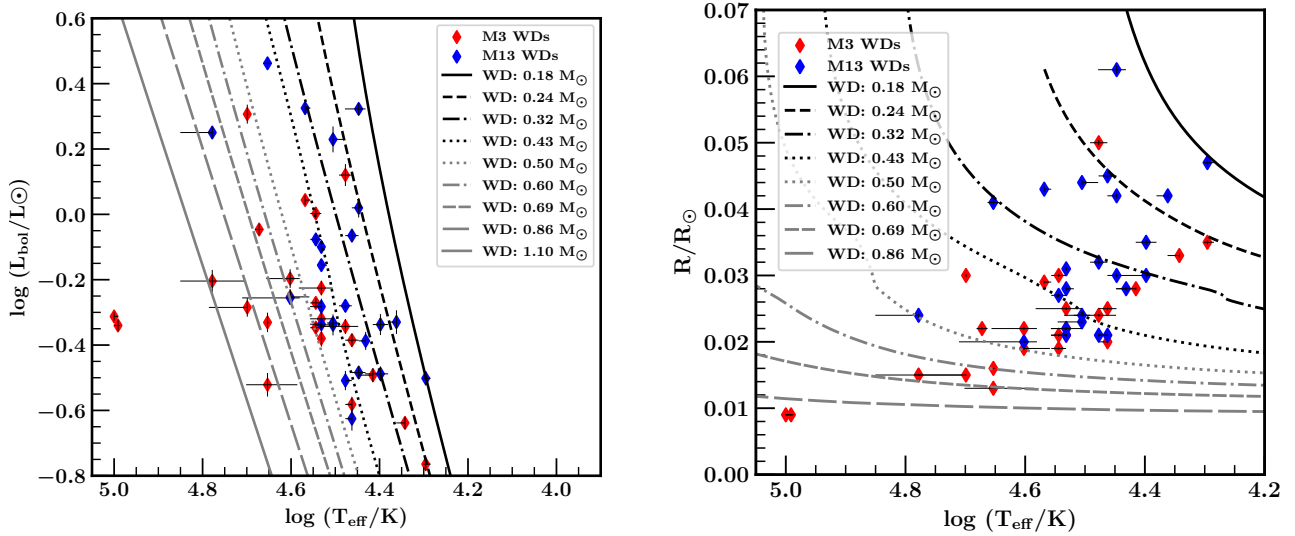


Figure 7. T_{eff} vs luminosity (left panel) and T_{eff} vs radius (right panel) of WDs of M3 (red diamonds) and M13 (blue diamonds). The cooling sequences of WDs in the mass range $0.18 - 1.10 M_{\odot}$ are shown in different styles and colours as mentioned in the legends.

photometric fluxes in UVIT and *HST* (UBVRI) filters for the inner (outer) region of the clusters. The SED fitting was performed in VO SED Analyzer¹ (Bayo et al. 2008, hereafter VOSA) where we have used Kurucz stellar atmosphere model (Castelli et al. 1997; Castelli & Kurucz 2003) for bHB, iHB, eHB, and post-HB stars, and Tubingen NLTE Model Atmosphere Package (TMAP) Grid2 (Grid for

$H=1.0$, $\lambda_{\text{max}} \sim 4.0 \times 10^5 \text{ \AA}$, $20,000 \text{ K} < T_{\text{eff}} < 150,000 \text{ K}$) model (Werner & Dreizler 1999; Werner et al. 2003; Rauch & Deetjen 2003) for eHB and post-HB stars. The best-fitted model parameters including the radial distance from the cluster center for the HB and post-HB stars are provided in Tables 2, 3, and 4.

In Figure 6, we show the T_{eff} vs L_{bol} plots of HB and post-HB stars along with BaSTI-IAC ZAHB locus for $Y = 0.247$ and 0.300 , and post-ZAHB evolutionary tracks for various HB masses (similar to those shown in Figure 5).

¹ <http://svo2.cab.inta-csic.es/theory/vosa/>

We find 2 eHB stars of M13 (ID: 73 and 600) lying well above the TAHB locus ($L_{\text{bol}} \sim 1.65 L_{\odot}$ and $1.85 L_{\odot}$) which suggests that they have already evolved from their HB phase to post-HB phase. We have added them in the list of post-HB stars of M13 (Table 4). We also see 2 more eHB stars (ID: 453 and 713) of M13 lying close to the TAHB locus ($L_{\text{bol}} \sim 1.55 L_{\odot}$ and $1.60 L_{\odot}$) which indicates that they might have almost completed their He-core burning stage and are about to evolve from their HB phase.

Out of three post-HB stars of M3, two are near the post-HB evolutionary track for M_{HB} of $0.49 M_{\odot}$ and the other one is near the post-HB evolutionary track of M_{HB} of $0.52 M_{\odot}$ (brown solids in the left panel of Figure 6). We found that the two AGB-manqué stars identified by Schiavon et al. (2012) in M3 are evolved from M_{HB} of $0.49 M_{\odot}$. The post-HB stars of M13 can be found between post-HB evolutionary tracks of M_{HB} of $0.481 M_{\odot}$ and $0.55 M_{\odot}$ (right panel of Figure 6). We also found the L_{bol} of one post-HB star (ID: 272) below the TAHB locus ($L_{\text{bol}} \sim 1.45 L_{\odot}$), so we excluded this star from the list of post-HB stars.

6 WDS OF M3 AND M13

Using UVIT observations, Sahu et al. (2022) provided a catalogue of 107 WD candidates detected in 11 GCs. In FUV–optical CMDs, they lie below the eHB in a vertical sequence. We have considered the sources observed in similar regions of FUV–optical CMDs of M3 and M13 (Figure 2) as WDs candidates. We obtained a total of 27 WD candidates in M13 and 29 in M3. They show a narrow spread in F148W–F606W colour (-3.2 to -1.4 mag) in the inner region whereas those observed in the outer region show a relatively larger spread (-2.6 to 1.0 mag) in the F148W–V colour.

We performed SED fitting on WD candidates of M3 and M13 using observed photometric fluxes in UVIT and *HST* (UBVRI) filters for the inner (outer) region of the clusters. The SED fitting was performed using two WD models, Koester WD models (Koester 2010), and Levenhagen WD models (Levenhagen et al. 2017). Out of 56 WD candidates identified in M3 and M13, we could perform SED fitting only on 48 candidates using WD models (out of 48 WDs, 24 each are in M3 and M13). The SED-fitted stellar parameters of WD candidates of M3 and M13 are given in Tables 5 and 6, respectively. Their T_{eff} , L_{bol} , and radii are in the range of $19,750 - 100,000$ K ($19,750 - 60,000$ K), $0.172 - 2.026 L_{\odot}$ ($0.237 - 2.899 L_{\odot}$), and $0.009 - 0.050 R_{\odot}$ ($0.020 - 0.061 R_{\odot}$), respectively. In Figure 7, we show their T_{eff} vs. L_{bol} (left panel) and T_{eff} vs. radius (right panel) for WD candidates of M3 and M13 in red and blue colours, respectively. We find WD candidates of M3 to be hotter and smaller in size when compared to those of M13 (median T_{eff} of M3 and M13 are 35,000 and 31,000 K, respectively; median WD radii of M3 and M13 are 0.022 and $0.03 R_{\odot}$, respectively).

We have also shown the WD cooling sequences in the mass-range $0.18 - 1.10 M_{\odot}$. The cooling sequences of extremely low mass (ELM) He-core WDs ($0.15 \leq M/M_{\odot} \leq 0.43$) are taken from Althaus et al. (2013) which are generated by computing the non-conservative evolution of a binary system consisting of an initially $1.0 M_{\odot}$ zero-age main-sequence (ZAMS) star and a $1.4 M_{\odot}$ neutron star for various

initial orbital periods. The cooling tracks of CO-core WDs were taken from Renedo et al. (2010) for WD mass range $0.50 - 0.86 M_{\odot}$. These cooling tracks are derived from normal single stellar evolution. The cooling tracks for massive WDs ($1.06 - 1.28 M_{\odot}$) were obtained from Althaus et al. (2007) which are computed under partial degenerate conditions of core carbon burning of WDs.

The masses of WDs were estimated from the cooling tracks on the T_{eff} vs. L_{bol} plot (left panel of Figure 7). For candidates lying in between the cooling tracks, we assigned their masses as the mean mass of both the nearest cooling tracks. We have listed the estimated mass of WDs of M3 and M13 in Tables 5 and 6. The WD candidates of M3 and M13 appear to have masses $0.18 M_{\odot}$ or higher. There are 7 WD candidates of M3 and 12 WD candidates of M13 lying within the ELM WD cooling sequence ($M_{\text{WD}} \leq 0.43 M_{\odot}$) whereas 15 WD candidates of both M3 and M13 have masses in the range, $0.43 - 0.50 M_{\odot}$ such that they could be formed through single or binary evolution. In M3, 5 WD candidates have masses of more than $0.86 M_{\odot}$. Out of them, 2 are with $M_{\text{WD}} \sim 0.86 M_{\odot}$ and one with $M_{\text{WD}} \sim 1.1 M_{\odot}$ which burn carbon in partially degenerate conditions. The rest 2 WD candidates having $\log(T_{\text{eff}}/\text{K}) \sim 5.0$ are hotter than any WD cooling sequence to be fitted, hence, we could not predict their evolutionary status.

Although Chen et al. (2021) studied the WDs of M3 and M13, their study was only focused on the WDs with masses $0.5 - 0.6 M_{\odot}$ (single star evolution). In this paper, we see that WDs with such masses are less in number (Chen et al. 2021) and also suggested that the WD counts would be very less in number at higher luminosities. However, WDs evolved from the binary evolution would stay longer at higher luminosities and will have low masses than the single stellar evolution WDs (Althaus et al. 2013). This scenario may be supported by the fact that we see more than 53% of HB stars lying below the ZAHB locus (Figure 6) which may be blue-hook stars (a result of hot flasher scenario from the binary system at RGB phase; Lei et al. 2015, 2016) and as a result, they may end up with low mass He-core WDs which is the case we see in M13 compared to M3. It is also possible that the WDs from single-star evolution could cool faster than the low-mass WDs, and therefore become fainter rapidly beyond the detection limit of UVIT. This may also cause a reduction in the detected number of these WDs. In either case, this study presents the detection of low-mass WD candidates in M3 and M13.

7 SUMMARY

Below we summarise the results and conclusions of this study:

- We have studied the HB, post-HB, and hot WDs of M3 and M13 GCs using UVIT observations in two FUV filters in combination with the *HST* WFC3 filters for the inner region and the ground-based UBVR photometry for the outer region of the cluster.
- We detected a total of 663 and 217 HB stars in UVIT filters for M13 and M3, respectively. The HB stars were further divided into three sub-populations, bHB, iHB, and eHB, based upon their T_{eff} in the range $7.75 - 11.5$ kK, $11.5 - 20$ kK, and $20 - 30$ kK, respectively.

- We used synthetic colours of HB stars to find the He-spread for bHB, iHB, and eHB sub-populations of M13 as 0.247 – 0.256, 0.26 – 0.30, and 0.29 – 0.31, respectively. The bHB of M3 has a He-spread of 0.252 – 0.266. We found 3 and 31 post-HB stars in M3 and M13, respectively. Their evolutionary tracks on CMDs as well as T_{eff} vs. L_{bol} plane suggest that they have evolved from $M_{\text{HB}} \leq 0.55 M_{\odot}$.

- The comparison of synthetic and observed colours of HB stars suggests that the mass-loss at RGB and initial He-spread in both clusters have a simultaneous effect on the different HB distributions observed in M3 and M13. e.g., HB stars of M13 require a larger spread in Y as well as ΔM . M13 with a larger fraction of eHB and iHB stars than M3 can only be simulated if HB distribution of M13 has higher values of Y and ΔM .

- We compared the derived He-abundances and RGB mass-loss with the latest available estimates obtained using multiple populations analysis by [Milone et al. \(2018\)](#); [Tailo et al. \(2019, 2020\)](#) and for the clusters, the values match well within the present uncertainties/indetermination. We found that the observed blue HB stars of M13 are the progeny of 1G, 2G, and 2Ge RGB populations whereas the observed blue HB stars of M3 are the progeny of 2G RGB populations.

- We detected 24 WD candidates each in M3 and M13. Their parameters have a large range (T_{eff} , L_{bol} , and stellar radii in the range 19,750–100,000 K (19,750–60,000 K), 0.172–2.026 L_{\odot} (0.237–2.899 L_{\odot}), 0.009–0.050 R_{\odot} (0.020–0.061 R_{\odot}), respectively, for M3 (M13)).

- The WD cooling sequences obtained from single, binary, and massive star evolution when over-plotted on the T_{eff} vs. L_{bol} and T_{eff} vs. stellar radii diagram suggest that some of the FUV detected WD candidates of M13 could be evolved from binary stellar evolution (lying on ELM cooling sequences), whereas most of the FUV detected WD candidates of M3 follow single stellar evolution.

ACKNOWLEDGEMENTS

We thank the referee for his/her suggestions which improved the content and readability of our manuscript. RK would like to acknowledge CSIR Research Fellowship (JRF) Grant No. 09/983(0034)/2019-EMR-1 for financial support. ACP and SP acknowledge the support of Indian Space Research Organisation (ISRO) under *AstroSat* archival Data utilization program. This publication uses the data from the *AstroSat* mission of the ISRO, archived at the Indian Space Science Data Center (ISSDC). AS acknowledges support from SERB Power Fellowship. DKO acknowledges the support of the Department of Atomic Energy, Government of India, under Project Identification No. RTI 4002. ACP also thanks Inter University centre for Astronomy and Astrophysics (IUCAA), Pune, India for providing facilities under associate-ship programs.

DATA AVAILABILITY

The data underlying this article will be shared upon reasonable request to the corresponding author.

REFERENCES

- Althaus L. G., García-Berro E., Isern J., Córscico A. H., Rohrmann R. D., 2007, *A&A*, **465**, 249
- Althaus L. G., Miller Bertolami M. M., Córscico A. H., 2013, *A&A*, **557**, A19
- Althaus L. G., Camisassa M. E., Miller Bertolami M. M., Córscico A. H., García-Berro E., 2015, *A&A*, **576**, A9
- Bayo A., Rodrigo C., Barrado Y Navascués D., Solano E., Gutiérrez R., Morales-Calderón M., Allard F., 2008, *A&A*, **492**, 277
- Behr B. B., 2003, *ApJS*, **149**, 67
- Bond H. E., 2021, *AJ*, **161**, 204
- Brown T. M., et al., 2016, *ApJ*, **822**, 44
- Cardelli J. A., Clayton G. C., Mathis J. S., 1989, *ApJ*, **345**, 245
- Cassisi S., Salaris M., 2020, *A&ARv*, **28**, 5
- Castelli F., Kurucz R. L., 2003, in Piskunov N., Weiss W. W., Gray D. F., eds, *IAUS Vol. 210, Modelling of Stellar Atmospheres*. p. A20 ([arXiv:astro-ph/0405087](#))
- Castelli F., Gratton R. G., Kurucz R. L., 1997, *A&A*, **318**, 841
- Catelan M., de Freitas Pacheco J. A., 1995, *A&A*, **297**, 345
- Chen J., Ferraro F. R., Cadelano M., Salaris M., Lanzoni B., Pallanca C., Althaus L. G., Dalessandro E., 2021, *Nature Astronomy*, **5**, 1170
- Dalessandro E., Salaris M., Ferraro F. R., Mucciarelli A., Cassisi S., 2013, *MNRAS*, **430**, 459
- Davis B. D., Bond H. E., Siegel M. H., Ciardullo R., 2022, *ApJ*, **926**, 99
- Denissenkov P. A., Vandenberg D. A., Kopacki G., Ferguson J. W., 2017, *ApJ*, **849**, 159
- Dotter A., 2013, *Mem. Soc. Astron. Italiana*, **84**, 97
- Ferraro F. R., Carretta E., Corsi C. E., Fusi Pecci F., Cacciari C., Buonanno R., Paltrinieri B., Hamilton D., 1997, *A&A*, **320**, 757
- Grundahl F., Vandenberg D. A., Andersen M. I., 1998, *ApJ*, **500**, L179
- Grundahl F., Catelan M., Landsman W. B., Stetson P. B., Andersen M. I., 1999, *ApJ*, **524**, 242
- Harris W. E., 1996, *AJ*, **112**, 1487
- Koester D., 2010, *Mem. Soc. Astron. Italiana*, **81**, 921
- Kumar R., Pradhan A. C., Parthasarathy M., Ojha D. K., Mohapatra A., Murthy J., Cassisi S., 2021a, *Journal of Astrophysics and Astronomy*, **42**, 36
- Kumar R., Pradhan A. C., Mohapatra A., Moharana A., Ojha D. K., Parthasarathy M., Murthy J., 2021b, *MNRAS*, **502**, 313
- Kumar R., Pradhan A. C., Parthasarathy M., Piridi S., Cassisi S., Ojha D. K., Mohapatra A., Murthy J., 2022, *MNRAS*, **511**, 5070
- Laget M., Burgarella D., Milliard B., Donas J., 1992, *A&A*, **259**, 510
- Lardo C., Salaris M., Cassisi S., Bastian N., 2022, *A&A*, **662**, A117
- Lardo C., Salaris M., Cassisi S., Bastian N., Mucciarelli A., Cabrera-Ziri I., Dalessandro E., 2023, *A&A*, **669**, A19
- Legnardi M. V., et al., 2022, *MNRAS*, **513**, 735
- Lei Z., Chen X., Zhang F., Han Z., 2015, *MNRAS*, **449**, 2741
- Lei Z., Zhao G., Zeng A., Shen L., Lan Z., Jiang D., Han Z., 2016, *MNRAS*, **463**, 3449
- Levenhagen R. S., Diaz M. P., Coelho P. R. T., Hubeny I., 2017, *ApJS*, **231**, 1
- Marino A. F., et al., 2014, *MNRAS*, **437**, 1609
- Marino A. F., et al., 2019, *MNRAS*, **487**, 3815
- Miller Bertolami M. M., Althaus L. G., García-Berro E., 2013, *ApJ*, **775**, L22
- Milone A. P., Marino A. F., 2022, *Universe*, **8**, 359
- Milone A. P., et al., 2014, *ApJ*, **785**, 21
- Milone A. P., et al., 2017, *MNRAS*, **464**, 3636
- Milone A. P., et al., 2018, *MNRAS*, **481**, 5098

- Moehler S., 2010, *Mem. Soc. Astron. Italiana*, **81**, 838
- Moehler S., Landsman W. B., Sweigart A. V., Grundahl F., 2003, *A&A*, **405**, 135
- Moehler S., Landsman W. B., Lanz T., Miller Bertolami M. M., 2019, *A&A*, **627**, A34
- Momany Y., Piotto G., Recio-Blanco A., Bedin L. R., Cassisi S., Bono G., 2002, *ApJ*, **576**, L65
- Momany Y., Bedin L. R., Cassisi S., Piotto G., Ortolani S., Recio-Blanco A., De Angeli F., Castelli F., 2004, *A&A*, **420**, 605
- Nardiello D., et al., 2018, *MNRAS*, **481**, 3382
- Newell E. B., 1970, *ApJ*, **159**, 443
- Paltrinieri B., Ferraro F. R., Carretta E., Fusi Pecci F., 1998, *MNRAS*, **293**, 434
- Peterson R. C., 1983, *ApJ*, **275**, 737
- Pietrinferni A., Cassisi S., Salaris M., Castelli F., 2006, *ApJ*, **642**, 797
- Pietrinferni A., et al., 2021, *ApJ*, **908**, 102
- Prabhu D. S., Subramaniam A., Sahu S., 2021, *ApJ*, **908**, 66
- Rauch T., Deetjen J. L., 2003, in Hubeny I., Mihalas D., Werner K., eds, *Astronomical Society of the Pacific Conference Series Vol. 288, Stellar Atmosphere Modeling*. p. 103 ([arXiv:astro-ph/0403239](https://arxiv.org/abs/astro-ph/0403239))
- Renedo I., Althaus L. G., Miller Bertolami M. M., Romero A. D., Córscico A. H., Rohrmann R. D., García-Berro E., 2010, *ApJ*, **717**, 183
- Rood R. T., 1973, *ApJ*, **184**, 815
- Sahu S., Subramaniam A., Côté P., Rao N. K., Stetson P. B., 2019, *MNRAS*, **482**, 1080
- Sahu S., et al., 2022, *MNRAS*, **514**, 1122
- Sandage A., Wildey R., 1967, *ApJ*, **150**, 469
- Schiavon R. P., et al., 2012, *AJ*, **143**, 121
- Schlafly E. F., Finkbeiner D. P., 2011, *ApJ*, **737**, 103
- Singh G., Sahu S., Subramaniam A., Yadav R. K. S., 2020, *ApJ*, **905**, 44
- Stetson P. B., Pancino E., Zocchi A., Sanna N., Monelli M., 2019, *MNRAS*, **485**, 3042
- Tailo M., D'Antona F., Caloi V., Milone A. P., Marino A. F., Lagioia E., Cordoni G., 2019, *MNRAS*, **486**, 5895
- Tailo M., et al., 2020, *MNRAS*, **498**, 5745
- Vasiliev E., Baumgardt H., 2021, *MNRAS*, **505**, 5978
- Werner K., Dreizler S., 1999, *Journal of Computational and Applied Mathematics*, **109**, 65
- Werner K., Deetjen J. L., Dreizler S., Nagel T., Rauch T., Schuh S. L., 2003, in Hubeny I., Mihalas D., Werner K., eds, *Astronomical Society of the Pacific Conference Series Vol. 288, Stellar Atmosphere Modeling*. p. 31 ([arXiv:astro-ph/0209535](https://arxiv.org/abs/astro-ph/0209535))
- Whitney J. H., et al., 1995, *AJ*, **110**, 1722

This paper has been typeset from a $\text{\TeX}/\text{\LaTeX}$ file prepared by the author.

Table 2. Stellar parameters along with their associated errors of 217 HBs of M3 and 678 HBs of M13 derived from SED fitting. The eT_{eff} and eT_{effm} columns are the upper and lower limits of error in T_{eff} . The complete table will be available online.

Cluster	Phase	ID	RA (degree)	DEC (degree)	Teff (K)	eT_{eff} (K)	eT_{effm} (K)	logg (dex)	elogg (dex)	L (L_{\odot})	eL (L_{\odot})	R (R_{\odot})	eR (R_{\odot})	Model	Radial distance (arcsec)
M3	bHB	27	205.44031	28.29328	9250.0	250.0	0.0	2.7	0.51	39.433	0.917	2.446	0.0197	Kurucz2003alp	456.9
M3	bHB	28	205.4633	28.2767	7750.0	500.0	0.0	3.15	0.84	45.032	1.577	3.718	0.03	Kurucz2003	451.5
M3	bHB	34	205.36681	28.40855	8000.0	250.0	0.0	1.9	1.04	41.055	0.886	3.335	0.0269	Kurucz2003alp	586.1
M3	bHB	63	205.4456	28.39114	8500.0	250.0	250.0	2.8	1.03	43.934	1.761	3.055	0.0246	Kurucz2003alp	329.4
M3	bHB	68	205.4977	28.33659	8000.0	250.0	0.0	2.55	1.25	42.871	0.93	3.415	0.0275	Kurucz2003	217.4

Table 3. Stellar parameters along with their associated errors of 3 post-HBs of M3 derived from SED fitting.

ID	RA (degree)	DEC (degree)	Teff (K)	eT_{eff} (K)	eT_{effm} (K)	logg (dex)	elogg (dex)	L (L_{\odot})	eL (L_{\odot})	R (R_{\odot})	eR (R_{\odot})	Model	Radial distance (arcsec)
92	205.52431	28.31793	30000.0	0.0	2000.0	6.35	0.55	89.171	1.634	0.349	0.0028	tmap1	226.9
174	205.5049	28.39036	27000.0	1000.0	1000.0	6.1	0.62	86.836	1.62	0.425	0.0034	tmap1	145.7
196	205.5928	28.28496	5500.0	0.0	250.0	3.65	0.9	179.776	3.488	14.759	0.1189	Kurucz2003alp	360.9

Table 4. Stellar parameters of 31 post-HBs of M13 derived from SED fitting. Star ID 73 and 600 are added in the list of post-HB stars on the basis of their position in the post-HB region in the $\log T_{\text{eff}}$ vs. $\log L_{\text{bol}}$ plane.

ID	RA (degree)	DEC (degree)	Teff (K)	eT_{eff} (K)	eT_{effm} (K)	logg (dex)	elogg (dex)	L (L_{\odot})	eL (L_{\odot})	R (R_{\odot})	eR (R_{\odot})	Model	Radial distance (arcsec)
19	250.43491	36.36537	28000.0	30000.0	1000.0	5.5	2.29	46.889	1.817	0.29	0.003	tmap2	342.3
73	250.4579	36.39996	42000.0	15000.0	6000.0	4.05	0.15	46.462	0.994	0.128	0.0013	tmap2	239.6
139	250.40021	36.4326	17000.0	1000.0	0.0	4.85	0.23	75.757	1.981	1.008	0.0103	Kurucz2003alp	116.4
374	250.39349	36.45731	24000.0	1000.0	0.0	3.45	0.47	114.338	2.698	0.612	0.0063	Kurucz2003	82.6
423	250.4183	36.45238	8250.0	500.0	0.0	2.1	0.62	98.036	2.175	4.806	0.0492	Kurucz2003alp	28.8
428	250.3956	36.45974	34000.0	1000.0	1000.0	4.0	0.0	62.785	3.367	0.228	0.0023	Kurucz2003alp	76.0
441	250.39751	36.45974	34000.0	2000.0	3000.0	3.9	0.2	57.31	2.14	0.219	0.0022	Kurucz2003	70.4
492	250.4493	36.44659	32000.0	1000.0	1000.0	4.2	0.4	48.775	1.789	0.227	0.0023	Kurucz2003alp	92.8
521	250.4314	36.45312	9250.0	250.0	0.0	3.25	0.78	87.663	1.984	3.649	0.0374	Kurucz2003	36.8
600	250.3828	36.47147	44000.0	12000.0	3000.0	4.0	0.0	71.268	1.521	0.144	0.0015	tmap2	120.5
603	250.2832	36.50146	15000.0	0.0	0.0	3.8	0.9	88.492	2.262	1.396	0.0143	Kurucz2003	428.3
575	250.44	36.45331	8250.0	250.0	0.0	1.7	0.64	165.451	3.722	6.297	0.0645	Kurucz2003alp	57.7
620	250.4585	36.44939	17000.0	0.0	1000.0	4.8	0.33	78.27	2.921	1.019	0.0104	Kurucz2003alp	112.7
671	250.4241	36.46192	18000.0	0.0	0.0	3.3	0.87	53.725	1.554	0.754	0.0077	Kurucz2003alp	9.9
684	250.4384	36.45827	21000.0	0.0	1000.0	3.75	0.78	71.279	2.726	0.639	0.0065	Kurucz2003alp	48.3
774	250.342	36.49117	19000.0	0.0	1000.0	3.75	0.84	52.243	1.458	0.672	0.0069	Kurucz2003alp	257.1
753	250.4156	36.46846	9000.0	250.0	0.0	2.3	0.75	103.918	2.311	4.194	0.043	Kurucz2003	35.8
794	250.4182	36.46939	8250.0	500.0	0.0	2.2	0.81	104.518	2.474	4.993	0.0511	Kurucz2003alp	35.9
929	250.35921	36.49708	19000.0	0.0	1000.0	4.1	0.92	83.429	2.497	0.847	0.0087	Kurucz2003alp	225.4
875	250.43629	36.46927	31000.0	0.0	1000.0	3.55	0.15	96.84	2.674	0.341	0.0035	Kurucz2003alp	53.8
941	250.39461	36.48714	12000.0	250.0	750.0	5.0	0.0	189.535	4.853	3.194	0.0327	Kurucz2003alp	125.9
947	250.411	36.48284	20000.0	0.0	1000.0	3.7	1.08	68.718	1.848	0.697	0.0071	Kurucz2003alp	88.5
955	250.4122	36.48304	32000.0	2000.0	2000.0	3.75	0.25	75.788	2.861	0.284	0.0029	Kurucz2003alp	88.0
958	250.42909	36.47835	12250.0	250.0	250.0	3.25	0.84	117.174	3.109	2.406	0.0246	Kurucz2003alp	69.8
974	250.39751	36.48886	14000.0	0.0	1000.0	4.05	0.76	64.549	1.662	1.364	0.014	Kurucz2003alp	125.9
1068	250.45441	36.48516	23000.0	8000.0	1000.0	6.45	2.45	68.387	2.183	0.518	0.0053	tmap2	131.1
1115	250.4016	36.51425	8500.0	250.0	0.0	2.0	0.5	111.766	2.826	4.849	0.0497	Kurucz2003alp	204.4
1147	250.4494	36.52553	33000.0	5000.0	3000.0	4.05	0.15	154.973	11.45	0.378	0.0039	tmap2	249.5
1156	250.49001	36.51987	15000.0	0.0	0.0	4.4	0.49	72.32	1.78	1.268	0.013	Kurucz2003alp	292.6
1164	250.2112	36.61396	42000.0	9000.0	3000.0	4.45	0.15	176.72	17.836	0.249	0.0026	tmap2	824.0
1180	250.5022	36.5579	32000.0	4000.0	6000.0	4.6	1.48	122.214	8.07	0.357	0.0037	tmap2	422.7

Table 5. Stellar parameters along with the associated errors of 24 WDs of M3 derived from SED fitting. The eMassp and eMassm columns are the upper and lower limits of error in WD mass.

ID	RA (degree)	DEC (degree)	Teff (K)	eTeffp (K)	eTeffm (K)	logg (dex)	elogg (dex)	L (L_{\odot})	eL (L_{\odot})	R (R_{\odot})	eR (R_{\odot})	Model	Radial distance (arcsec)	Mass (M_{\odot})	eMassp (R_{\odot})	eMassm (R_{\odot})
57	205.4805	28.33584	19750.0	250.0	500.0	9.3	0.19	0.172	0.008	0.035	3.0E-4	koester2	261.8	0.24	0.01	0.01
71	205.4675	28.37843	22000.0	1000.0	0.0	8.32	0.45	0.23	0.01	0.033	3.0E-4	koester2	256.3	0.28	0.04	0.04
223	205.5278	28.37083	45000.0	0.0	0.0	7.62	0.72	0.467	0.032	0.016	1.0E-4	koester2	69.3	0.78	0.08	0.08
232	205.52299	28.37996	29000.0	1000.0	0.0	8.82	0.45	0.262	0.014	0.02	2.0E-4	koester2	81.1	0.47	0.035	0.01
266	205.53951	28.36581	30000.0	1000.0	1000.0	9.34	0.14	1.319	0.102	0.05	4.0E-4	levenhagen17	50.0	0.28	0.04	0.04
291	205.52631	28.38557	34000.0	4000.0	2000.0	9.32	0.2	0.595	0.031	0.025	2.0E-4	koester2	76.1	0.47	0.035	0.035
352	205.54311	28.37141	100000.0	0.0	2000.0	7.53	0.14	0.487	0.014	0.009	1.0E-4	levenhagen17	27.0	99.0	99.0	99.0
361	205.5479	28.36636	98000.0	2000.0	1000.0	7.32	0.28	0.457	0.017	0.009	1.0E-4	levenhagen17	39.3	99.0	99.0	99.0
474	205.5365	28.38878	47000.0	1000.0	1000.0	9.37	0.11	0.899	0.035	0.022	2.0E-4	levenhagen17	56.0	0.65	0.05	0.05
619	205.54179	28.39195	29000.0	1000.0	1000.0	9.18	0.28	0.412	0.019	0.025	2.0E-4	koester2	56.8	0.395	0.035	0.035
652	205.55	28.38515	60000.0	10000.0	10000.0	6.9	0.34	0.625	0.049	0.015	1.0E-4	koester2	28.8	1.1	0.24	0.24
661	205.56799	28.36277	50000.0	10000.0	0.0	7.0	0.35	0.519	0.034	0.015	1.0E-4	koester2	81.1	0.86	0.24	0.01
672	205.5647	28.36751	45000.0	5000.0	7000.0	9.25	0.25	0.301	0.025	0.013	1.0E-4	koester2	62.4	0.98	0.12	0.12
761	205.5547	28.38568	35000.0	1000.0	1000.0	7.45	0.31	0.536	0.018	0.021	2.0E-4	koester2	36.2	0.47	0.035	0.035
798	205.56129	28.38363	30000.0	4000.0	2000.0	9.32	0.2	0.454	0.024	0.024	2.0E-4	koester2	46.7	0.395	0.035	0.035
811	205.5656	28.37999	34000.0	2000.0	2000.0	9.25	0.25	0.479	0.025	0.022	2.0E-4	koester2	55.3	0.47	0.035	0.035
826	205.56329	28.38589	35000.0	1000.0	1000.0	6.82	0.28	0.45	0.016	0.019	2.0E-4	koester2	56.4	0.5	0.01	0.01
844	205.5614	28.39203	40000.0	0.0	4000.0	6.9	0.34	0.559	0.031	0.019	2.0E-4	koester2	67.2	0.6	0.01	0.01
868	205.5081	28.46718	35000.0	1000.0	1000.0	8.18	0.65	1.006	0.035	0.03	2.0E-4	koester2	347.9	0.395	0.035	0.035
1050	205.6338	28.42872	37000.0	0.0	1000.0	7.21	0.16	1.106	0.038	0.029	2.0E-4	levenhagen17	327.7	0.44	0.035	0.035
1055	205.5993	28.48572	26000.0	2000.0	0.0	9.1	0.3	0.322	0.016	0.028	2.0E-4	koester2	422.3	0.34	0.02	0.02
1112	205.5349	28.35661	50000.0	0.0	0.0	7.62	0.72	2.026	0.136	0.03	2.0E-4	koester2	85.8	0.55	0.05	0.05
1134	205.54939	28.39877	34000.0	0.0	0.0	8.75	0.29	0.417	0.024	0.021	2.0E-4	levenhagen17	77.4	0.5	0.01	0.01
1135	205.55901	28.39784	40000.0	5000.0	2000.0	9.15	0.32	0.636	0.042	0.022	2.0E-4	koester2	81.3	0.55	0.05	0.05

Table 6. Stellar parameters of 24 WDs of M13 derived from SED fitting.

ID	RA (degree)	DEC (degree)	Teff (K)	eTeffp (K)	eTeffm (K)	logg (dex)	elogg (dex)	L (L_{\odot})	eL (L_{\odot})	R (R_{\odot})	eR (R_{\odot})	Model	Radial distance (arcsec)	Mass (M_{\odot})	eMassp (R_{\odot})	eMassm (R_{\odot})
6	250.4462	36.34667	29000.0	1000.0	0.0	7.24	0.2	0.237	0.02	0.021	2.0E-4	levenhagen17	413.6	0.47	0.035	0.035
36	250.3822	36.39391	19750.0	250.0	500.0	8.32	0.22	0.315	0.016	0.047	5.0E-4	koester2	263.7	0.182	0.01	0.01
45	250.33501	36.41498	34000.0	2000.0	0.0	6.82	0.28	0.522	0.029	0.022	2.0E-4	koester2	298.9	0.21	0.03	0.03
46	250.25591	36.43906	27000.0	1000.0	0.0	8.6	0.49	0.41	0.026	0.028	3.0E-4	koester2	486.3	0.34	0.02	0.02
74	250.5079	36.38501	32000.0	3000.0	0.0	6.85	0.32	0.459	0.034	0.023	2.0E-4	koester2	367.1	0.47	0.035	0.035
149	250.26241	36.47466	25000.0	1000.0	1000.0	9.1	0.34	0.46	0.034	0.035	4.0E-4	koester2	464.6	0.28	0.04	0.04
193	250.4158	36.43419	40000.0	10000.0	2000.0	9.25	0.25	0.555	0.022	0.02	2.0E-4	koester2	94.1	0.6	0.26	0.1
287	250.4319	36.4391	45000.0	1000.0	1000.0	9.34	0.14	2.899	0.111	0.041	4.0E-4	levenhagen17	80.2	0.47	0.035	0.035
289	250.40359	36.44783	34000.0	2000.0	0.0	9.2	0.24	0.461	0.019	0.021	2.0E-4	koester2	68.3	0.47	0.035	0.035
390	250.4189	36.45007	28000.0	1000.0	1000.0	9.37	0.11	0.328	0.015	0.03	3.0E-4	levenhagen17	36.3	0.395	0.035	0.035
408	250.4214	36.45056	34000.0	0.0	1000.0	7.21	0.16	0.699	0.026	0.028	3.0E-4	levenhagen17	33.5	0.47	0.035	0.035
413	250.3933	36.45935	32000.0	1000.0	1000.0	7.16	0.14	0.465	0.019	0.024	2.0E-4	levenhagen17	82.6	0.47	0.035	0.035
434	250.4135	36.4547	34000.0	0.0	0.0	9.05	0.29	0.795	0.035	0.031	3.0E-4	levenhagen17	30.5	0.43	0.01	0.01
554	250.44569	36.45067	25000.0	2000.0	1000.0	9.2	0.24	0.325	0.017	0.03	3.0E-4	koester2	76.6	0.32	0.01	0.01
687	250.41229	36.46652	60000.0	10000.0	0.0	7.22	0.6	1.78	0.072	0.024	3.0E-4	koester2	36.6	0.78	0.08	0.08
701	250.5107	36.43714	30000.0	0.0	1000.0	7.0	0.35	0.31	0.021	0.021	2.0E-4	koester2	270.0	0.47	0.01	0.01
712	250.4415	36.4586	35000.0	1000.0	1000.0	6.82	0.28	0.838	0.031	0.027	3.0E-4	koester2	57.1	0.47	0.035	0.035
760	250.4261	36.46552	37000.0	0.0	1000.0	9.21	0.24	2.114	0.09	0.043	4.0E-4	levenhagen17	23.8	0.32	0.01	0.01
772	250.4393	36.46181	28000.0	2000.0	1000.0	9.3	0.19	2.102	0.091	0.061	6.0E-4	koester2	51.1	0.21	0.03	0.03
860	250.43311	36.46903	29000.0	1000.0	1000.0	9.34	0.14	0.861	0.038	0.045	5.0E-4	levenhagen17	46.4	0.28	0.04	0.04
1051	250.43739	36.48792	30000.0	1000.0	1000.0	9.36	0.13	0.525	0.022	0.032	3.0E-4	levenhagen17	110.6	0.36	0.01	0.01
1160	250.3826	36.55949	28000.0	1000.0	0.0	7.03	0.39	1.047	0.071	0.042	4.0E-4	koester2	376.2	0.24	0.01	0.01
1166	250.5157	36.52699	32000.0	0.0	2000.0	8.68	0.52	1.696	0.155	0.044	4.0E-4	koester2	363.6	0.28	0.04	0.04
1184	250.52251	36.56129	23000.0	1000.0	0.0	8.52	0.55	0.468	0.039	0.042	4.0E-4	koester2	467.1	0.21	0.03	0.03